Spatial and longitudinal tracking of enhancer-AAV vectors that target transgene expression to injured mouse myocardium

David W. Wolfson[1, 2], Joshua A. Hull[2], Yongwu Li[4], Trevor J. Gonzalez[2], Mourya D. Jayaram[2], Garth W. Devlin[2], Valentina Cigliola[1, 3], Kelsey A. Oonk[1], Alan Rosales[4], Nenad Bursac[4], Aravind Asokan[2]*, and Kenneth D. Poss[1, 5, 6]*

[1]Duke Regeneration Center, Department of Cell Biology, Duke University School of Medicine, Durham, NC, USA
[2]Department of Surgery, Duke University School of Medicine, Durham, NC, USA
[3]Department of Pharmacology, Vanderbilt University, Nashville, TN, USA
[4]Department of Biomedical Engineering, Duke University, Durham, NC, USA
[5]Morgridge Institute for Research, Madison, WI, USA
[6]Department of Cell & Regenerative Biology, University of Wisconsin-Madison, Madison, WI, USA

*Authors for correspondence (aravind.asokan@duke.edu; kposs@morgridge.org)

ABSTRACT

Tissue regeneration enhancer elements (TREEs) direct expression of target genes in injured and regenerating tissues. Additionally, TREEs of zebrafish origin were shown to direct the expression of transgenes in border zone regions after cardiac injury when packaged into recombinant AAV vectors and introduced into mice. Future implementation of TREEs into AAV-based vectors as research tools and potential gene therapy modalities will require a more detailed understanding of expression dynamics and potential off-target effects. Here, we applied in vivo bioluminescent imaging to mice systemically injected with AAV vectors containing different combinations of capsids, enhancers, and timing of delivery. Longitudinal tracking of TREE-based expression over time revealed distinct amplitudes and durations of reporter gene expression in the injured heart directed by different TREEs. The liver-de-targeted AAV capsid, AAV.cc84, was able to deliver TREEs either pre- or post-cardiac injury to negate off-target expression in the liver while maintaining transduction in the heart. By screening AAV9-based capsid libraries dosed systemically in mice post-cardiac injury, we discovered a new capsid variant, AAV.IR41, with enhanced transduction at cardiac border zone regions, and with elevated transduction of TREE driven transgenes versus conventional AAV9 vectors. In vivo bioluminescence imaging offers insights into how enhancers and engineered capsids can be implemented to modulate spatiotemporal transgene expression for future targeted therapies.

Keywords: regeneration, heart, AAV capsids, gene expression, enhancer

INTRODUCTION

The inability of the adult mammalian heart to regenerate after an infarction injury has motivated attempts to discover factors with cardiomyogenic, angiogenic, or anti-fibrotic potential. Many genes have been implicated by genetic studies in zebrafish and mouse to elevate or restrict cardiomyocyte (CM) proliferation after cardiac injury, with groups targeting factors controlling differentiation, chromatin state, metabolism, and other events (Eulalio et al., 2012; Choi et al., 2013; Fang et al., 2013; Mahmoud et al., 2013; Karra et al., 2015; Bassat et al., 2017; Toischer et al., 2017; Hirose et al., 2019; Chen et al., 2021; Li et al., 2023; Nguyen et al., 2023). Notable mitogenic influences include the secreted factor Neuregulin1 (Nrg1), signaling through ErbB family receptors (Bersell et al., 2009; D'Uva et al., 2015; Gemberling et al., 2015), the transcription factor (TF) Klf1 (Ogawa et al., 2021), and Yap/Taz factors, normally restrained from the nucleus by Hippo in CMs (von Gise et al., 2012; Heallen et al., 2013; Xin et al., 2013; Morikawa et al., 2015; Bassat et al., 2017; Leach et al., 2017; Morikawa et al., 2017; Monroe et al., 2019). The signaling environment is complex, with epicardium, endocardium, nerves, macrophages, T cells, vasculature, and oxygen levels each influencing CM regeneration (Lepilina et al., 2006; Kim et al., 2010; Kikuchi et al., 2011; Aurora et al., 2014; Mahmoud et al., 2015; Wang et al., 2015; Hui et al., 2017; Nakada et al., 2017; Sugimoto et al., 2017; Zhao et al., 2019; Xia et al., 2022; Peterson et al., 2024; Shin et al., 2024; Sun et al., 2024; Weinberger et al., 2024).

It has become crucial to decipher how genes involved in regenerative events engage upon injury in CMs and other cardiac cells. Recently, distal regulatory elements referred to as tissue regeneration enhancer elements (TREEs) were described that direct gene expression in regenerating zebrafish hearts, a new concept for the field of regenerative biology (Kang et al., 2016). TREEs have been identified by chromatin profiling in CMs, epicardium, and other tissues of zebrafish like spinal cord and fins (Goldman et al., 2017; Thompson et al., 2020; Cao et al., 2022; Cigliola et al., 2023), as well as in a variety of other species, tissues, and injury contexts (Harris et al., 2016; Vizcaya-Molina et al., 2018; Gehrke et al., 2019; Harris et al., 2020; Wang et al., 2020; Jimenez et al., 2022; Sun et al., 2022; Suzuki et al., 2022; Li et al., 2023; Sun and Poss, 2023; Zlatanova et al., 2023; Kawaguchi et al., 2024). Critically, TREEs of zebrafish origin can be recognized by the transcriptional machinery of small (mice)

or even large (pigs) mammals. Systemic introduction of adeno-associated viral (AAV) vectors with TREE-cargo cassettes can spatiotemporally target factor delivery to the injured mammalian heart or spinal cord (Cigliola et al., 2023; Yan et al., 2023). For instance, a TREE paired with a heavily mutated YAP transgene transiently directs expression to the border zone of a mouse heart injured by ischemia/reperfusion, stimulating localized CM cycling and functional recovery (Yan et al., 2023). Thus, short TREE sequences found in zebrafish, and presumably elements with similar properties from other organisms, can act as targeting vehicles for regenerative augmentation.

Critical remaining questions include how TREEs interact with target genes and TFs, and how they can be harnessed for safe regenerative applications. Translational use of TREEs for delivering pro-regenerative factors requires optimized delivery systems to maximize efficacy and safety while minimizing off-target risks. Recently, new engineered and variant forms of adeno-associated virus (AAV) capsids have been developed to modulate tissue tropism and cell type specificity, such as liver de-targeting with AAV.cc84 (Gonzalez et al., 2023). Here, we performed a study to assess how choice of TREE and AAV capsid can influence the spatiotemporal control of transgene expression in mouse models of myocardial infarction (MI). Using bioluminescence imaging, we mapped and longitudinally tracked AAV transgene expression in a whole-body manner and screened for new variant AAV9 capsids with enhanced tropism for infarcted myocardial tissue over healthy myocardium.

RESULTS AND DISCUSSION

IVIS detects TREE-directed gene expression after myocardial injury

We previously showed that TREEs are capable of directing AAV transgene expression in an injury-responsive manner in mouse models of spinal cord and cardiac damage (Cigliola et al., 2023; Yan et al., 2023). In these studies, TREEs were placed upstream of a murine *Heat shock protein 68* (*Hsp68*) promoter, normally silent in mouse tissues, and a EGFP reporter transgene, and AAV vectors were delivered systemically. EGFP transgene expression to observe TREE activity could not be longitudinally tracked in individual mice, limiting our ability to observe whole-body spatial distribution of expression (on- and off-target).

To longitudinally monitor AAV transgene expression using in vivo bioluminescence imaging (IVIS), albino BALB/c mice were injected intravenously with AAV9 containing either a chicken *beta actin* (*CBA*) or *Hsp68* promoter upstream of a firefly *luciferase* (*fLuc*) transgene (Fig. S1A). As expected the strong, constitutively active *CBA* promoter directed robust fLuc expression across the mouse body, whereas mice transduced with AAV9 harboring *Hsp68:fLuc* had relatively minimal luminescence, mostly originating from the liver (Fig. S1B). Luminescence in the heart, liver, and whole body plateaued and remained stable from 30-68 days post-AAV delivery for both *CBA* and *Hsp68* vectors, as indicated by average radiance measurement (Fig. S1C-E).

To determine if IVIS detected gene expression directed by zebrafish TREE sequences in injured mouse tissues, we then systemically delivered AAV9 vectors containing *Hsp68::fLuc* with or without a TREE sequence 60 days prior to ischemia/reperfusion (I/R) or sham surgery. This 60-day period was intended to allow AAV expression to stabilize prior to surgery (Fig. 1A). We employed two TREEs that previously indicated different injury responsiveness and temporal dynamics by histology, the *runx1*-linked enhancer (REN) and the *2ankrd1a*-linked enhancer *2ankrd1a* (Goldman et al., 2017). Transduction of either TREE sequence resulted in a marked increase in bioluminescence signal in the thoracic cage overlying the heart. Bioluminescence peaked within the first 3 days after I/R and returned to pre-injury baseline levels within 35 days post-injury (dpi) (Fig. 1B, C; n = 2 mice). Cardiac bioluminescence showed no change after sham surgery for all mice, indicating that TREE-directed expression occurred in response to myocardial trauma (Fig. 1D). Notably, each AAV vector (*CBA*, *Hsp68*, and TREE) demonstrated off-target expression in the abdominal region directly above the liver after transduction, which was also indicated to a limited degree by histology in our previous study (Fig. 1B, S1B) (Yan et al., 2023).

Live imaging of a liver de-targeted AAV9 capsid variant

To attempt to reduce hepatic transgene expression while maintaining cardiac tropism, we packaged *REN-Hsp68::fLuc* into AAV.cc84, a recently discovered AAV9 variant with reduced liver transduction (Gonzalez et al., 2023), as well as AAV9 for comparison. *REN* was selected as the liver luminescence

was more prominent with respect to the cardiac signal in above experiments. Following AAV delivery, mice were imaged weekly and also given a sham surgery at day 28, to assess spatiotemporal dynamics of bioluminescence (Fig. 2A). IVIS images revealed off-target luminescence in male and female livers with AAV9, whereas AAV.cc84 showed no detectable signal in the liver for all sexes of mice over 35-days following AAV (Fig. 2B, S2A). Quantification indicated that AAV9 enabled substantially higher expression in liver than AAV.cc84, which remained minimal over time (Fig. 2C, n = 6 mice). Luminescence in the heart was similar between AAV9 and AAV.cc84, and, as expected, luminescence showed no change upon sham surgery (Fig. S2B). Six-weeks post-AAV, while AAV.cc84-injected mice continued to show minimal expression across many biopsied organs, AAV9-injected mice showed off-target expression in the liver (Fig. 2D). Vector genome quantification by qPCR revealed AAV9-injected mice contained a much higher viral load in liver tissue compared to AAV.cc84, for both males and females (Fig. 2E, n = 3 mice). Vector genomes in the heart were similar between AAV9 and AAV.cc84 for both sexes of mice (Fig. S2C). In addition to heart and liver, luminescence was also observed in the head/neck and lower abdomen regions, which showed no difference between AAV9 and AAV.cc84 (Fig. S2D, E). These results indicate that AAV.cc84 can be implemented to minimize off-target liver expression of TREEs, evading liver transduction while maintaining cardiac tropism.

Live imaging of post injury, liver de-targeted TREE-AAV transduction

Therapeutic TREE use would require their delivery after injury occurs. To examine expression dynamics in a therapeutically-relevant context, we systemically delivered the liver-detargeted vector AAV.cc84 carrying *2ankrd1aEN-Hsp68::fLuc* or *Hsp68::fLuc* at 4 dpi in mice given an ischemia-reperfusion (I/R) injury (Fig. 3A). Echocardiograms to measure cardiac ejection fraction before and after I/R were used to estimate and compare injury size in both treatment groups (Fig. S3A). *2ankrd1aEN-Hsp68::fLuc*-transduced mice showed robust fLuc expression in the thoracic cage overlying the heart, which increased up to 28 dpi and plateaued afterwards (Fig. 3B, C; n = 4 mice). Conversely, cardiac bioluminescence in *Hsp68::fLuc*-transduced mice remained relatively minimal over time (Figs. 3B, C

and S3B, n = 4 mice). IVIS imaging revealed a baseline of *2ankrd1aEN*-directed cardiac expression in sham-operated mice (Fig. S3C), which was elevated ~3-fold in mice with I/R injury compared to sham at 7 dpi (Fig. 3D, n = 4 mice). *2ankrd1aEN*-directed bioluminescence in the heart increased during the first 28 days for sham-operated mice, likely indicative of increased AAV transduction and transgene expression over time (noting that AAV deliveries in Figure 1 experiments were 60 days prior to luminescence measurements; Fig. 3E). Notably, I/R injured mice maintained higher cardiac expression throughout the 63-day time course, with the greatest differences at 7 and 21 dpi (Fig. 3E). Together, these results indicate that *2ankrd1aEN*-directed gene expression can be estimated longitudinally over long time, and in agreement with our previous histological analysis, *2ankrd1aEN* directs long-lasting gene expression in the injured mouse heart.

In vivo library screen for AAV9 capsid variants with increased targeting of injury sites

Directed evolution of AAV libraries have been previously used to discover new capsids with improved functional properties, such as liver de-targeting (AAV.cc84), enhanced potency (AAV.cc47), and tropism for specific cell types (AAV.ark313, AAV.k20) (Gonzalez et al., 2022; Gonzalez et al., 2023; Nyberg et al., 2023; Nyberg et al., 2025; Rosales et al., 2025). We reasoned that this approach may be useful to identify variants with enhanced tropism for infarcted myocardium, which has altered extracellular matrix and cell type landscapes.

To find capsid variants with enhanced tropism for infarcted myocardial tissue over healthy myocardium, we incorporated previously described AAV capsid libraries with saturation mutagenesis at the variable region IV epitope (Gonzalez et al., 2023). A previous report indicated that AAV9 is observed to preferentially transduce border zones of infarcted myocardium when delivered acutely (10 minutes to 3 dpi) after injury, which was speculated to be driven by a combination of increased capillary permeability, sialidase activity, and DNA damage after cardiac ischemia (Konkalmatt et al., 2012). We attempted to limit the effects of these acute changes by delivering capsid libraries to mice that had undergone sham or I/R surgery at 9 dpi, when the acute inflammation phase is complete and the repair phase with myofibroblast activation and proliferation has begun (Fig. 4A, n = 2 mice). At 11 dpi, cardiac

tissue was harvested and separate biopsies were acquired from infarcted or remote myocardium. Viral genomes from each biopsy were amplified and sequenced, and infarcted tissue fold-change over remote tissue was calculated from mapped reads for each capsid variant (Fig. 4B). We found 3 unique capsids that were enriched in the infarcted tissue over remote for both I/R mice, while being comparably expressed in both biopsies of the sham mouse (Fig. 4B, S4A). Of the 3 variant capsids, we found the capsid with the highest number of reads in infarcted tissue (AAV.IR41) transduced I/R-injured hearts more effectively than AAV9 and the other two variant capsids (IR42, IR43) when packaged with a *CBA::EGFP* transgene (Fig. 4C, S4B). When systemically delivered at 9 dpi, IR41 transduced larger areas of myocardium surrounding areas of infarct compared to AAV9 (Fig. 4C). Using F-actin stain to mark the border zone, AAV9 and IR41 primarily transduced cardiomyocytes directly at the border zone with similar effectiveness (Fig. 4C). EGFP did not notably co-localize with vimentin staining of non-myocytes for either AAV9 or IR41, thus both capsids still primarily transduce CM (Fig. S4C). Thus, sequence-based screening identified a capsid with enhanced transduction and expression in injured myocardium.

IR41 capsid delivery of TREE-directed transgene expression in injured hearts

To assess the efficacy of TREE-directed transgene targeting using IR41 capsid, we systemically transduced mice at 4 days after permanent left coronary artery ligation (MI) with either AAV9 or IR41 harboring a *2ankrd1aEN-Hsp68::fLuc* transgene. IVIS imaging revealed higher expression levels in animals transduced with IR41 compared to AAV9, in both sham and MI groups (Figs. 5A and S5A; n = 3 mice). We also noted higher hepatic expression in both sham and infarcted mice with IR41 compared to AAV9 (Fig. 5A), although no new tissue transduction was introduced as detectable by biodistribution and reporter gene expression. The average and maximum radiances recorded in IR41-transduced mouse hearts were significantly higher than AAV9 by 7 dpi and remained elevated at 21 dpi (Fig. 5B, C). In mice that underwent sham surgery, IR41 had a higher average and maximum radiance than AAV9 at 7 dpi alone but was relatively similar at 14 and 21 dpi (Fig. S5B, C). Vector genome quantification by qPCR showed that IR41 had roughly twice as high viral uptake than AAV9 in mice

given cardiac injuries (Fig. 5D, n = 3 mice). Interestingly IR41-transduced mice showed a trend toward higher cardiac viral genome loads than AAV9-transduced mice upon sham injury, indicating that IR41 might increase tropism in uninjured hearts, but its effects will be greatest when delivered to injured hearts (Fig. 5D). Together, our experiments indicate that increased tropism of AAV.IR41 for injured myocardium, defined by enhanced uptake and higher transgene expression versus control AAV9, can be complemented by injury-responsive TREEs for targeting cargo delivery to sites of cardiac damage.

Conclusions and limitations

Here, we report techniques for spatial and longitudinal tracking of injury- and regeneration-responsive, TREE-directed transgene expression from AAV vectors systemically infused into mice, either pre- or post injury. We characterized whole-body temporal dynamics of TREE-directed AAV expression and how expression may be modulated with the incorporation of engineered capsids, including those that may better target injured tissue. Our study indicates that IVIS imaging for assessing amplitude and specificity of TREE-directed transgene expression will aid future development of enhancer-based gene therapies relevant to cardiac regeneration and disease. With an IVIS imaging modality, effects of capsid alterations and enhancer sequence alterations can be efficiently and noninvasively assessed to refine their ability to target gene expression in the injured heart.

There are several limitations we point out from these techniques. Expression by internal organs must also be approximated with potentially subjective ROIs that cannot be verified until harvesting the organs at sacrifice. Although the expression is approximated, we were able to observe unexpected off-target TREE expression in the liver, neck, and abdomen, which was modulated by capsid engineering. Additionally, future work exploring cell surface markers or receptors is needed to better understand the apparent enhanced tropism of IR41 over AAV9, and to engineer liver detargeting attributes into this form. For instance, it is possible that combining the modifications in AAV.cc84 and AAV.IR41 would produce additive effects. Finally, larger animal models are not suited for IVIS imaging due to limitations of tissue penetrance, and findings in mice may not fully recapitulate those in larger animal models and humans. Our AAV capsid library screening was limited to mice, and capsid hits remain to be tested in

other species. While further optimization is required, this work lays a foundation for refining TREE-targeted factor delivery to injured myocardium and expanding their use in applications for therapeutic tissue repair.

MATERIALS AND METHODS

Animal husbandry

All mouse protocols were approved by the Institutional Animal Care and Use Committee (IACUC) at Duke University (Protocols #A003-22-01, #A025-24-01), which is accredited by the Association for Assessment and Accreditation of Laboratory Animal Care-International (AAALAC). All mice were housed and maintained in the Duke University DLAR mouse facility. Wild-type male and female C57BL/6J (The Jackson Laboratory, Strain #:000664) and BALB/c (Charles River) mice were used for this study.

Ischemia/reperfusion and LAD ligation injury models

The procedure for I/R myocardial injury via temporary LCA ligation was adapted from previously described protocols (Kaiser et al., 2005). Briefly, adult mice, 8-12 weeks of age, were anesthetized with ketamine/xylazine, intubated and placed on a rodent ventilator. The chest cavity was entered in the third intercostal space at the left lateral border. The left atrium was gently deflected out of the field to expose the left anterior descending artery. Coronary ligation was performed by tying an 8-0 nylon suture ligature around the proximal LAD artery. Occlusion of the LAD was confirmed by the anterior wall of the left ventricle turning a pale color. LAD occlusion was maintained for 40 minutes. After the ischemia period, the suture was untied, and reperfusion of the LAD was confirmed by the return of a pink-red color to the anterior wall. The procedures for LAD ligation were performed with the same approach but with permanent ligation of the left coronary artery by tying an 8-0 nylon suture ligature around the proximal LAD artery. Occlusion of the LAD was confirmed by the anterior wall of the left ventricle turning a pale color. The chest was then closed, and the mice were extubated and allowed to recover from anesthesia. Mice were given post-operative analgesics (buprenorphine-sustained release formula by s.c. injection at 0.1 mg/kg) and allowed to recover until the experimental time points indicated, at which point mice were then further analyzed or tissues were harvested. I/R procedures were performed in the Duke Cardiovascular Physiology Core. LAD ligation procedures were performed in collaboration with Dr. Bursac's lab at Duke University.

Echocardiography

To assess cardiac function before and after injury, mice were anesthetized by 2% isoflurane inhalation and imaged by B-mode and M-mode echocardiography using a Vevo3100LT instrument with a 25–55 MHz transducer (MX550D, VisualSonics). At least 5x short axis M-mode traces of 8–10 seconds were recorded across the mid-papillary region of the LV. Systole and diastole LV dimensions were measured using VevoLab's Auto LV analysis tool. All measurements were averaged for each heart at each time point. Heart function was measured by calculating ejection fraction (EF) from the following formula: EF(%) = 100*[(LVED–LVES)/LVED], where LVED = $[7.0/(2.4+LVIDd)]*(LVIDd)^3$ and LVES = $[7.0/(2.4+LVIDs)]*(LVIDs)^3$. Abbreviations, LVED, left ventricular end-diastolic volume; LVES, left ventricular end-systolic volume; LVIDd, left ventricular internal dimension at end-diastole; LVIDs, left ventricular internal dimension at end-systole.

AAV capsid library

AAV9-based capsid libraries were constructed using saturation mutagenesis of residues within the VR-IV site as previously described (Gonzalez et al., 2023; Rosales et al., 2025). The parental library plasmid, containing AAV2 *ITR*s flanking AAV2 *Rep* and AAV9 *Cap* genes (pTR-wtAAV9-VR-IV), was generated with degenerate primers flanking the VR-IR region (amino acids 452-458 in *Cap*). Prior to saturation mutagenesis with degenerate primers, the VR-IV region of *Cap* was replaced with a partial *GFP* sequence to prevent incorporation of wild-type VR-IV sequences in the parental library. The parental library insert was incorporated into the pTR-wtAAV9-VR-IV plasmid to replace the *GFP* sequence via restriction enzyme digestion with XbaI and BsiWI followed by ligation (New England Biolabs). Purified ligation products were electroporated into DH10B ElectroMax cells (Invitrogen #18290015) and immediately plated on 245 mm Square BioAssay dishes (Corning #431111) containing LB agar with ampicillin. Plates were incubated at 32 °C overnight to allow colony growth and formation. The following day colonies were pooled and harvested for plasmid DNA collection via ZymoPURE plasmid MaxiPrep kit (Zymo Research, #D402). Purified library plasmids were co-transfected with

adenovirus helper plasmid into adherent HEK293 cells to generate AAV9 capsid libraries as described below.

AAV vector production and dosing

Recombinant AAV vectors and libraries were prepared using adherent or suspension HEK293 cell cultures as previously described (Gonzalez et al., 2022; Gonzalez et al., 2023; Rosales et al., 2025). For AAV libraries, at 80-90% confluency in 150 cm tissue culture dishes (Fisher Scientific, #087726), cells were triple transfected via polyethylenimine (PEI, Sigma-aldrich) in a 1:3 DNA:PEI ratio, containing transfer plasmid (pITR), adenovirus helper plasmid (pXX680), and RepCap plasmid (AAV9, AAV.cc84, or AAV.IR41). Cell media was harvested at days 4 and 6 post-transfection. For recombinant AAV vectors, suspension HEK293 cells generated in-house at Duke University were used. Similar to adherent transfection, suspension cells were triple-plasmid-transfected with PEI, containing pITR (0.3 ug/mL), pXX680 (0.6 ug/mL), and RepCap (0.5 ug/mL). Media was harvested at 6 days post-transfection with cells pelted and discarded by centrifugation. Both adherent and suspension AAV packaging workflows follow the same downstream purification processes. Briefly, harvested media was incubated with 12% polyethylene glycol (PEG) overnight at 4 °C. Media was then centrifuged at 4,000 x G at 4 °C for 45 minutes to precipitate PEG containing AAV. PEG was resuspended in AAV formulation buffer, containing 1 mM MgCl2 and 0.001% F-68 in dPBS. Resuspended PEG and AAV was DNase treated at 37 °C for 1 hour, followed by iodixanol gradient purification via ultracentrifugation at 30,000 RPM at 17 °C overnight. Iodixanol gradients consisted of 60%, 40%, 25%, and 17% densities. Following centrifugation, 550 ul fractions were collected starting from the 25%-40% border and ending at the 40%-60% border. All fractions were titered for AAV by qPCR using primers targeting the ITR region (Table 1). Iodixanol fractions containing the highest titer were selected for downstream desalting and buffer exchange. Desalting was performed using manufacturer's instructions with a PD MidiTrap G-25 column (Cytiva). Following desalting, buffer exchange with sterile AAV formulation buffer was performed according to manufacturer's instructions with a Pierce high-capacity endotoxin removal spin column (Thermo Scientific). Purified final AAV titer was measured by QIAcuity Digital PCR (dPCR)

system with QIAcuity probes targeting AAV2-ITR (Qiagen, #250102). Titered AAV was systemically delivered in 8-12-week-old mice via retro-orbital injection. AAV dose was calculated as viral genomes per kilogram body weight to account for body size differences across age and sex.

In vivo AAV capsid library screening in mice

The parental AAV9 capsid library for the VR-IV region was titered by qPCR using primers targeting the ITR region (Table 1). Parental libraries were systemically delivered to adult C57BL/6J mice (The Jackson Laboratory, #000664) that had undergone sham (n = 1) or I/R (n = 2) surgeries at 9 dpi. Sufficient cardiac injury by I/R was confirmed by echocardiography measurements of left ventricular ejection fraction. All mice were dosed with $2.5*10^{13}$ v.g./kg b.w. of the parental library. Two days after library delivery, at 11 dpi, all mice were sacrificed, and hearts were separately biopsied at the injury (infarct and border zone) and remote sites (right ventricle). Sham mice had heart biopsies captured from approximately the same areas, although no infarct was present. Injured and remote collected tissues were digested with Proteinase K for DNA isolation using a PureLink Genomic DNA mini kit (Invitrogen #K182002). AAV genomes were amplified from the genomic DNA using PCR primers targeting the AAV9 *Cap* gene (Table 1). Amplified AAV9 *Cap* sequences were then ligated into our AAV library plasmid backbone (pTR-wtAAV9-VR-IV) and used to generate a second AAV library. The parental and second viral libraries for all biopsies (remote, injured) and mice (sham, I/R) were prepared for high throughput sequencing to assess sequence diversity and enrichment. All viral libraries were Dnase I-treated prior to extraction of viral genome from the capsid, and subsequently fortified with Illumina adapter and index sequences by PCR. All PCR products were purified using the PureLink PCR micro kit (Invitrogen). Prepared libraries were then prepared for sequencing with the Illumina NovaSeq 6000 S-Prime Reagent Kit and sequenced with the Illumina NovaSeq system. Demultiplexed reads were analyzed with an updated in-house Perl script (Gonzalez et al., 2022; Gonzalez et al., 2023; Rosales et al., 2025). Reads are surveyed for nucleotide sequences flanking the AAV9 VR-IV library region and intermediate sequences are counted and ranked. These nucleotide sequences are then translated, and the resulting amino acid sequences are also counted and ranked. Fold change

enrichment in the injury versus remote biopsy was calculated using normalized read counts for each amino acid sequence. Co-expressed amino acid sequences found in both I/R-injured mice were plotted against each other to find amino acid sequences with >100-fold injury enrichment in I/R-injured mice. Injury fold change over remote was then averaged for both I/R-injured mice and plotted against the injury fold change for the corresponding amino acid sequence found in the sham mouse. Scatterplots were generated using the R studio graphics package v3.5.2.

IVIS imaging

All IVIS bioluminescence imaging was conducted with adult albino BALB/c mice (Charles River) using equipment provided by the Duke Optical Molecular Imaging and Analysis shared resource (OMIA) core. D-luciferin, potassium salt (Gold Biotechnology) was dissolved in dPBS (without calcium or magnesium) at a final concentration of 15 mg/mL. The D-luciferin was sterile-filtered with a 0.22 um filter, and aliquots were stored frozen for future use. At each imaging timepoint, D-luciferin was thawed on ice in a covered container to protect from light. While mice were anesthetized under 2% isoflurane, thawed D-luciferin was injected intraperitoneally at 150 mg/kg b.w. dose. Regions of interest for this study, such as the heart and liver, had body hair above them removed using Nair to improve signal-noise ratio. Luciferase signals were allowed a 10-15-minute plateau time. Bioluminescence images were then collected using an IVIS Kinetic instrument and Living Image Software (PerkinElmer). Average and maximum radiances were quantified in specified regions of interest with the Living Image software. For ex vivo bioluminescence imaging, mice were sacrificed and organs immediately harvested for imaging. Organs were quickly washed with ice cold PBS and DMEM to remove blood and debris. After washing, organs were submerged in room temperature D-luciferin solution for 10 minutes, then immediately placed on black construction paper and imaged in the IVIS Kinetic.

Viral genome biodistribution

Genomic DNA was extracted from tissues using a PureLink Genomic DNA mini kit (Invitrogen #K182002) following manufacturer's instructions. Viral genomes were then quantified by qPCR with a

known DNA mass of pITR transfer plasmid standard used for AAV packaging. qPCR primers were designed to target the border region between the transgene and bgh-PolyA sequence (below). Quantified viral genomes are presented as a ratio of viral genomes per microgram of extracted genomic DNA used for the reaction.

Primers used in this study:

Name	**Sequence (5’ - 3’)**
ITR F	AACATGCTACGCAGAGAGGGAGTGG
ITR R	CATGAGACAAGGAACCCCTAGTGATGGAG
AAV9 lib amp F	AGCACGGTCCAGGTCTTCAC
AAV9 lib amp R	ATGTCAGTCTAGACCAAAGTTCAACTGAAACGAATTAAACGG
WPRE-bGH F	CTTCGCCCTCAGACGAGTCGGA
WPRE-bGH R	TGGCTGGCAACTAGAAGGCACA

Immunofluorescence

Adult mouse hearts were immediately harvested after sacrifice, perfused with room temperature dPBS (without calcium or magnesium), and fixed overnight in 4% paraformaldehyde (Fisher #50-980-487) at 4 °C. After fixing, hearts were washed in PBS three times for 15 minutes each and incubated in 30% sucrose in PBS overnight at 4 °C. Hearts were then transferred and embedded in Tissue-Plus OCT (Fisher #23-730-571). Tissue blocks were cryosectioned at 10 um and placed on a Superfrost™ Plus Microscope slide (Fisher #22-037-246). Slides were stored at -80 °C until staining. On day of staining, slides were thawed on a slide warmer and allowed to dry for 30 minutes. Tissues were rehydrated with PBS, washed 3x with PBS-T (PBS + 0.1% Triton X100), and then blocked for 1 hour at room temperature in PBS-T with 5% normal goat serum. After blocking, slides were incubated with primary antibodies diluted in antibody solution (PBS-T + 1% BSA) overnight in a humidified chamber at 4 °C. Primary antibodies included: anti-GFP (Invitrogen #A-11122) at 1:1000 dilution and anti-vimentin (DSHB #40E-C) at 1:100 dilution. Following primary antibody incubation, slides were washed 3x with PBS-T and incubated with secondary antibodies, DAPI (Thermo Scientific #62248, 1:1000 dilution), and

Alexa Fluor 546 Phalloidin (Invitrogen #A22283, 1:200 dilution) in antibody solution for 2 hours at room temperature. Secondary antibodies included: goat anti-rabbit IgG Alexa Fluor 488 (Invitrogen #A-11008) at 1:500 dilution and goat anti-mouse IgG Alexa Fluor 555 (Invitrogen #A-21422) at 1:500 dilution. Following incubation, slides were washed 3x with PBS for 5 minutes each and mounted with Vectashield HardSet Antifade Mounting media (Vector Laboratories #H-1400-10). Mounted slides were stored at 4 °C until imaged.

ACKNOWLEDGMENTS

We thank the Duke Cardiovascular Physiology Core for cardiac injuries. We acknowledge NIH for research funding (N.B.: R01EB 032726, R01HL164013, and U01HL134764; A.A.: R01HL089221, R01DK134408; K.D.P: R35 HL150713).

AUTHOR CONTRIBUTIONS

Conceptualization: D.W.W., N.B., A.A., K.D.P.; Methodology: D.W.W., J.A.H., Y.L., T.J.G., V.C., K.A.O., A.R., N.B.; Software: J.A.H.; Vector Production: M.D.J., G.W.D.; Formal analysis: D.W., J.A.H., T.J.G., A.R., M.J.D., G.W.D., A.A.; Investigation: D.W.; Resources: N.B., A.A., K.D.P.; Writing - original draft: D.W., K.D.P.; Writing - review & editing: D.W., N.B., A.A., K.D.P.; Visualization: D.W.; Supervision: A.A., K.D.P.; Project administration: K.D.P.; Funding acquisition: A.A., K.D.P.

REFERENCES

Aurora, A. B., Porrello, E. R., Tan, W., Mahmoud, A. I., Hill, J. A., Bassel-Duby, R., Sadek, H. A. and Olson, E. N. (2014) 'Macrophages are required for neonatal heart regeneration', *J Clin Invest* 124(3): 1382-92.

Bassat, E., Mutlak, Y. E., Genzelinakh, A., Shadrin, I. Y., Baruch-Umansky, K., Yifa, O., Kain, D., Rajchman, D., Leach, J., Bassat, D. R. et al. (2017) 'The extracellular matrix protein Agrin promotes heart regeneration in mice', *Nature* 547, 179-184..

Bersell, K., Arab, S., Haring, B. and Kuhn, B. (2009) 'Neuregulin1/ErbB4 signaling induces cardiomyocyte proliferation and repair of heart injury', *Cell* 138(2): 257-70.

Cao, Y., Xia, Y., Balowski, J. J., Ou, J., Song, L., Safi, A., Curtis, T., Crawford, G. E., Poss, K. D. and Cao, J. (2022) 'Identification of enhancer regulatory elements that direct epicardial gene expression during zebrafish heart regeneration', *Development* 149(4): dev200133.

Chen, Y., Luttmann, F. F., Schoger, E., Scholer, H. R., Zelarayan, L. C., Kim, K. P., Haigh, J. J., Kim, J. and Braun, T. (2021) 'Reversible reprogramming of cardiomyocytes to a fetal state drives heart regeneration in mice', *Science* 373(6562): 1537-1540.

Choi, W. Y., Gemberling, M., Wang, J., Holdway, J. E., Shen, M. C., Karlstrom, R. O. and Poss, K. D. (2013) 'In vivo monitoring of cardiomyocyte proliferation to identify chemical modifiers of heart regeneration', *Development* 140(3): 660-6.

Cigliola, V., Shoffner, A., Lee, N., Ou, J., Gonzalez, T. J., Hoque, J., Becker, C. J., Han, Y., Shen, G., Faw, T. D. et al. (2023) 'Spinal cord repair is modulated by the neurogenic factor Hb-egf under direction of a regeneration-associated enhancer', *Nat Commun* 14(1): 4857.

D'Uva, G., Aharonov, A., Lauriola, M., Kain, D., Yahalom-Ronen, Y., Carvalho, S., Weisinger, K., Bassat, E., Rajchman, D., Yifa, O. et al. (2015) 'ERBB2 triggers mammalian heart regeneration by promoting cardiomyocyte dedifferentiation and proliferation', *Nat Cell Biol* 17(5): 627-38.

Eulalio, A., Mano, M., Dal Ferro, M., Zentilin, L., Sinagra, G., Zacchigna, S. and Giacca, M. (2012) 'Functional screening identifies miRNAs inducing cardiac regeneration', *Nature* 492(7429): 376-81.

Fang, Y., Gupta, V., Karra, R., Holdway, J. E., Kikuchi, K. and Poss, K. D. (2013) 'Translational profiling of cardiomyocytes identifies an early Jak1/Stat3 injury response required for zebrafish heart regeneration', *Proc Natl Acad Sci U S A* 110(33): 13416-21.

Gehrke, A. R., Neverett, E., Luo, Y. J., Brandt, A., Ricci, L., Hulett, R. E., Gompers, A., Ruby, J. G., Rokhsar, D. S., Reddien, P. W. et al. (2019) 'Acoel genome reveals the regulatory landscape of whole-body regeneration', *Science* 363(6432):eaau6173..

Gemberling, M., Karra, R., Dickson, A. L. and Poss, K. D. (2015) 'Nrg1 is an injury-induced cardiomyocyte mitogen for the endogenous heart regeneration program in zebrafish', *Elife* 4:e05871.

Goldman, J. A., Kuzu, G., Lee, N., Karasik, J., Gemberling, M., Foglia, M. J., Karra, R., Dickson, A. L., Sun, F., Tolstorukov, M. Y. et al. (2017) 'Resolving Heart Regeneration by Replacement Histone Profiling', *Dev Cell* 40(4): 392-404 e5.

Gonzalez, T. J., Mitchell-Dick, A., Blondel, L. O., Fanous, M. M., Hull, J. A., Oh, D. K., Moller-Tank, S., Castellanos Rivera, R. M., Piedrahita, J. A. and Asokan, A. (2023) 'Structure-guided AAV capsid evolution strategies for enhanced CNS gene delivery', *Nat Protoc* 18(11): 3413-3459.

Gonzalez, T. J., Simon, K. E., Blondel, L. O., Fanous, M. M., Roger, A. L., Maysonet, M. S., Devlin, G. W., Smith, T. J., Oh, D. K., Havlik, L. P. et al. (2022) 'Cross-species evolution of a highly potent AAV variant for therapeutic gene transfer and genome editing', *Nat Commun* 13(1): 5947.

Harris, R. E., Setiawan, L., Saul, J. and Hariharan, I. K. (2016) 'Localized epigenetic silencing of a damage-activated WNT enhancer limits regeneration in mature Drosophila imaginal discs', *Elife* 5:e11588.

Harris, R. E., Stinchfield, M. J., Nystrom, S. L., McKay, D. J. and Hariharan, I. K. (2020) 'Damage-responsive, maturity-silenced enhancers regulate multiple genes that direct regeneration in Drosophila', *Elife* 9:e58305.

Heallen, T., Morikawa, Y., Leach, J., Tao, G., Willerson, J. T., Johnson, R. L. and Martin, J. F. (2013) 'Hippo signaling impedes adult heart regeneration', *Development* 140(23): 4683-90.

Hirose, K., Payumo, A. Y., Cutie, S., Hoang, A., Zhang, H., Guyot, R., Lunn, D., Bigley, R. B., Yu, H., Wang, J. et al. (2019) 'Evidence for hormonal control of heart regenerative capacity during endothermy acquisition', *Science* 364(6436): 184-188.

Hui, S. P., Sheng, D. Z., Sugimoto, K., Gonzalez-Rajal, A., Nakagawa, S., Hesselson, D. and Kikuchi, K. (2017) 'Zebrafish Regulatory T Cells Mediate Organ-Specific Regenerative Programs', *Dev Cell* 43(6): 659-672 e5.

Jimenez, E., Slevin, C. C., Song, W., Chen, Z., Frederickson, S. C., Gildea, D., Wu, W., Elkahloun, A. G., Ovcharenko, I. and Burgess, S. M. (2022) 'A regulatory network of Sox and Six transcription factors initiate a cell fate transformation during hearing regeneration in adult zebrafish', *Cell Genom* 2(9):100170.

Kaiser, R. A., Liang, Q., Bueno, O., Huang, Y., Lackey, T., Klevitsky, R., Hewett, T. E. and Molkentin, J. D. (2005) 'Genetic inhibition or activation of JNK1/2 protects the myocardium from ischemia-reperfusion-induced cell death in vivo', *J Biol Chem* 280(38): 32602-8.

Kang, J., Hu, J., Karra, R., Dickson, A. L., Tornini, V. A., Nachtrab, G., Gemberling, M., Goldman, J. A., Black, B. L. and Poss, K. D. (2016) 'Modulation of tissue repair by regeneration enhancer elements', *Nature* 532: 201-206.

Karra, R., Knecht, A. K., Kikuchi, K. and Poss, K. D. (2015) 'Myocardial NF-kappaB activation is essential for zebrafish heart regeneration', *Proc Natl Acad Sci U S A* 112(43): 13255-60.

Kawaguchi, A., Wang, J., Knapp, D., Murawala, P., Nowoshilow, S., Masselink, W., Taniguchi-Sugiura, Y., Fei, J. F. and Tanaka, E. M. (2024) 'A chromatin code for limb segment identity in axolotl limb regeneration', *Dev Cell* 59(16), 2239-2253.

Kikuchi, K., Holdway, J. E., Major, R. J., Blum, N., Dahn, R. D., Begemann, G. and Poss, K. D. (2011) 'Retinoic acid production by endocardium and epicardium is an injury response essential for zebrafish heart regeneration', *Dev Cell* 20(3): 397-404.

Kim, J., Wu, Q., Zhang, Y., Wiens, K. M., Huang, Y., Rubin, N., Shimada, H., Handin, R. I., Chao, M. Y., Tuan, T. L. et al. (2010) 'PDGF signaling is required for epicardial function and blood vessel formation in regenerating zebrafish hearts', *Proc Natl Acad Sci U S A* 107(40): 17206-10.

Konkalmatt, P. R., Wang, F., Piras, B. A., Xu, Y., O'Connor, D. M., Beyers, R. J., Epstein, F. H., Annex, B. H., Hossack, J. A. and French, B. A. (2012) 'Adeno-associated virus serotype 9 administered systemically after reperfusion preferentially targets cardiomyocytes in the infarct border zone with pharmacodynamics suitable for the attenuation of left ventricular remodeling', *J Gene Med* 14(9-10): 609-20.

Leach, J. P., Heallen, T., Zhang, M., Rahmani, M., Morikawa, Y., Hill, M. C., Segura, A., Willerson, J. T. and Martin, J. F. (2017) 'Hippo pathway deficiency reverses systolic heart failure after infarction', *Nature* 550(7675): 260-264.

Lepilina, A., Coon, A. N., Kikuchi, K., Holdway, J. E., Roberts, R. W., Burns, C. G. and Poss, K. D. (2006) 'A dynamic epicardial injury response supports progenitor cell activity during zebrafish heart regeneration', *Cell* 127(3): 607-19.

Li, L., Cui, L., Lin, P., Liu, Z., Bao, S., Ma, X., Nan, H., Zhu, W., Cen, J., Mao, Y. et al. (2023) 'Kupffer-cell-derived IL-6 is repurposed for hepatocyte dedifferentiation via activating progenitor genes from injury-specific enhancers', *Cell Stem Cell* 30(3): 283-299 e9.

Mahmoud, A. I., Kocabas, F., Muralidhar, S. A., Kimura, W., Koura, A. S., Thet, S., Porrello, E. R. and Sadek, H. A. (2013) 'Meis1 regulates postnatal cardiomyocyte cell cycle arrest', *Nature* 497(7448): 249-53.

Mahmoud, A. I., O'Meara, C. C., Gemberling, M., Zhao, L., Bryant, D. M., Zheng, R., Gannon, J. B., Cai, L., Choi, W. Y., Egnaczyk, G. F. et al. (2015) 'Nerves Regulate Cardiomyocyte Proliferation and Heart Regeneration', *Dev Cell* 34(4): 387-99.

Monroe, T. O., Hill, M. C., Morikawa, Y., Leach, J. P., Heallen, T., Cao, S., Krijger, P. H. L., de Laat, W., Wehrens, X. H. T., Rodney, G. G. et al. (2019) 'YAP Partially Reprograms Chromatin Accessibility to Directly Induce Adult Cardiogenesis In Vivo', *Dev Cell* 48(6): 765-779.

Morikawa, Y., Heallen, T., Leach, J., Xiao, Y. and Martin, J. F. (2017) 'Dystrophin-glycoprotein complex sequesters Yap to inhibit cardiomyocyte proliferation', *Nature* 547(7662): 227-231.

Morikawa, Y., Zhang, M., Heallen, T., Leach, J., Tao, G., Xiao, Y., Bai, Y., Li, W., Willerson, J. T. and Martin, J. F. (2015) 'Actin cytoskeletal remodeling with protrusion formation is essential for heart regeneration in Hippo-deficient mice', *Sci Signal* 8(375): ra41.

Nakada, Y., Canseco, D. C., Thet, S., Abdisalaam, S., Asaithamby, A., Santos, C. X., Shah, A. M., Zhang, H., Faber, J. E., Kinter, M. T. et al. (2017) 'Hypoxia induces heart regeneration in adult mice', *Nature* 541(7636): 222-227.

Nguyen, P. D., Gooijers, I., Campostrini, G., Verkerk, A. O., Honkoop, H., Bouwman, M., de Bakker, D. E. M., Koopmans, T., Vink, A., Lamers, G. E. M. et al. (2023) 'Interplay between calcium and sarcomeres directs cardiomyocyte maturation during regeneration', *Science* 380(6646): 758-764.

Nyberg, W. A., Ark, J., To, A., Clouden, S., Reeder, G., Muldoon, J. J., Chung, J. Y., Xie, W. H., Allain, V., Steinhart, Z. et al. (2023) 'An evolved AAV variant enables efficient genetic engineering of murine T cells', *Cell* 186(2): 446-460 e19.

Nyberg, W. A., Wang, C. H., Ark, J., Liu, C., Clouden, S., Qualls, A., Caryotakis, S., Wells, E., Simon, K., Garza, C. et al. (2025) 'In vivo engineering of murine T cells using the evolved adeno-associated virus variant Ark313', *Immunity* 58(2): 499-512 e7.

Ogawa, M., Geng, F. S., Humphreys, D. T., Kristianto, E., Sheng, D. Z., Hui, S. P., Zhang, Y., Sugimoto, K., Nakayama, M., Zheng, D. et al. (2021) 'Kruppel-like factor 1 is a core cardiomyogenic trigger in zebrafish', *Science* 372(6538): 201-205.

Peterson, E. A., Sun, J., Chen, X. and Wang, J. (2024) 'Neutrophils facilitate the epicardial regenerative response after zebrafish heart injury', *Dev Biol* 508: 93-106.

Rosales, A., Blondel, L. O., Hull, J., Gao, Q., Aykun, N., Peek, J. L., Vargas, A., Fergione, S., Song, M., Wilson, M. H. et al. (2025) 'Evolving adeno-associated viruses for gene transfer to the kidney via cross-species cycling of capsid libraries', *Nat Biomed Eng*.

Shin, K., Rodriguez-Parks, A., Kim, C., Silaban, I. M., Xia, Y., Sun, J., Dong, C., Keles, S., Wang, J., Cao, J. et al. (2024) 'Harnessing the regenerative potential of interleukin11 to enhance heart repair', *Nat Commun* 15(1): 9666.

Sugimoto, K., Hui, S. P., Sheng, D. Z. and Kikuchi, K. (2017) 'Dissection of zebrafish shha function using site-specific targeting with a Cre-dependent genetic switch', *Elife* 6:e24635.

Sun, F., Ou, J., Shoffner, A. R., Luan, Y., Yang, H., Song, L., Safi, A., Cao, J., Yue, F., Crawford, G. E. et al. (2022) 'Enhancer selection dictates gene expression responses in remote organs during tissue regeneration', *Nat Cell Biol* 24(5): 685-696.

Sun, F. and Poss, K. D. (2023) 'Inter-organ communication during tissue regeneration', *Development* 150(23):dev202166.

Sun, J., Peterson, E. A., Chen, X. and Wang, J. (2024) 'ptx3a(+) fibroblast/epicardial cells provide a transient macrophage niche to promote heart regeneration', *Cell Rep* 43(4): 114092.

Suzuki, N., Kanai, A., Suzuki, Y., Ogino, H. and Ochi, H. (2022) 'Adrenergic receptor signaling induced by Klf15, a regulator of regeneration enhancer, promotes kidney reconstruction', *Proc Natl Acad Sci U S A* 119(33): e2204338119.

Thompson, J. D., Ou, J., Lee, N., Shin, K., Cigliola, V., Song, L., Crawford, G. E., Kang, J. and Poss, K. D. (2020) 'Identification and requirements of enhancers that direct gene expression during zebrafish fin regeneration', *Development* 147(14):dev191262.

Toischer, K., Zhu, W., Hunlich, M., Mohamed, B. A., Khadjeh, S., Reuter, S. P., Schafer, K., Ramanujam, D., Engelhardt, S., Field, L. J. et al. (2017) 'Cardiomyocyte proliferation prevents failure in pressure overload but not volume overload', *J Clin Invest* 127(12): 4285-4296.

Vizcaya-Molina, E., Klein, C. C., Serras, F., Mishra, R. K., Guigo, R. and Corominas, M. (2018) 'Damage-responsive elements in Drosophila regeneration', *Genome Res* 28(12): 1852-1866.

von Gise, A., Lin, Z., Schlegelmilch, K., Honor, L. B., Pan, G. M., Buck, J. N., Ma, Q., Ishiwata, T., Zhou, B., Camargo, F. D. et al. (2012) 'YAP1, the nuclear target of Hippo signaling, stimulates heart growth through cardiomyocyte proliferation but not hypertrophy', *Proc Natl Acad Sci U S A* 109(7): 2394-9.

Wang, J., Cao, J., Dickson, A. L. and Poss, K. D. (2015) 'Epicardial regeneration is guided by cardiac outflow tract and Hedgehog signalling', *Nature* 522(7555): 226-30.

Wang, W., Hu, C. K., Zeng, A., Alegre, D., Hu, D., Gotting, K., Ortega Granillo, A., Wang, Y., Robb, S., Schnittker, R. et al. (2020) 'Changes in regeneration-responsive enhancers shape regenerative capacities in vertebrates', *Science* 369(6508):eaaz3090.

Weinberger, M., Simoes, F. C., Gungoosingh, T., Sauka-Spengler, T. and Riley, P. R. (2024) 'Distinct epicardial gene regulatory programs drive development and regeneration of the zebrafish heart', *Dev Cell* 59(3): 351-367 e6.

Xia, Y., Duca, S., Perder, B., Dundar, F., Zumbo, P., Qiu, M., Yao, J., Cao, Y., Harrison, M. R. M., Zangi, L. et al. (2022) 'Activation of a transient progenitor state in the epicardium is required for zebrafish heart regeneration', *Nat Commun* 13(1): 7704.

Xin, M., Kim, Y., Sutherland, L. B., Murakami, M., Qi, X., McAnally, J., Porrello, E. R., Mahmoud, A. I., Tan, W., Shelton, J. M. et al. (2013) 'Hippo pathway effector Yap promotes cardiac regeneration', *Proc Natl Acad Sci U S A* 110(34): 13839-44.

Yan, R., Cigliola, V., Oonk, K. A., Petrover, Z., DeLuca, S., Wolfson, D. W., Vekstein, A., Mendiola, M. A., Devlin, G., Bishawi, M. et al. (2023) 'An enhancer-based gene-therapy strategy for spatiotemporal control of cargoes during tissue repair', *Cell Stem Cell* 30(1): 96-111 e6.

Zhao, L., Ben-Yair, R., Burns, C. E. and Burns, C. G. (2019) 'Endocardial Notch Signaling Promotes Cardiomyocyte Proliferation in the Regenerating Zebrafish Heart through Wnt Pathway Antagonism', *Cell Rep* 26(3): 546-554 e5.

Zlatanova, I., Sun, F., Wu, R. S., Chen, X., Lau, B. H., Colombier, P., Sinha, T., Celona, B., Xu, S. M., Materna, S. C. et al. (2023) 'An injury-responsive mmp14b enhancer is required for heart regeneration', *Sci Adv* 9(48): eadh5313.

FIGURE LEGENDS

Figure 1. Longitudinal tracking of TREE-directed transgene expression in injured mice by IVIS
(A) Schematic illustration of study design. Albino BALB/c mice were systemically injected with AAV9 vectors packaging *fLuc* reporter cassettes directed by TREEs and a permissive promoter. Mice underwent I/R surgery at D61 and were imaged by IVIS at indicated time points**. (B)** Representative IVIS images indicate changes of expression over time and space for each vector. Cardiac region of interest (ROI) indicated by red box. n = 2 mice. **(C)** Average radiance measured from cardiac ROIs plotted over days post-injury (dpi). Average radiance normalized to their baseline pre-injury were also plotted (right). n = 2 mice. **(D)** Average cardiac radiance showed a transient increase in expression for both *REN* (left) and *2ankrd1aEN* (right) after I/R injury, whereas sham operated animals showed relatively constant expression. n = 2 mice for I/R, n = 3 mice for sham.

Figure 2. Liver-de-targeted AAV.cc84 capsid limits hepatic expression from TREEs
(A) Schematic of experimental timeline, comparing AAV9 and AAV.cc84 capsids for systemic delivery of *REN-Hsp68::fLuc*. Mice were IVIS imaged in the weeks following AAV delivery and post-sham surgery. **(B)** Representative IVIS images of mice injected with either AAV9 (left) or AAV.cc84 (right) at 14 (top) and 21 days (bottom) post-AAV injection. Mice were also subdivided by biological sex to account for sex differences in AAV liver tropism. **(C)** Average radiance from liver ROIs showed significantly higher expression in AAV9-transduced mice compared to AAV.cc84 through all timepoints (n = 6 mice, Holm-Sidak multiple comparisons test). **(D)** Representative IVIS images of harvested organs at 42 days post-AAV demonstrate liver expression with AAV9 (left) while undetected with AAV.cc84 (right). **(E)** Vector genome quantification from collected liver samples reveal higher liver transduction with AAV9 compared to AAV.cc84 for both female and male mice.

Figure 3. Post-injury delivery of AAV.cc84-packaged 2ankrd1aEN targets expression to cardiac injuries
(A) Schematic of experimental timeline comparing expression between *Hsp68* and *2ankrd1aEN* when delivered at 4 dpi. **(B)** Representative IVIS images of mice injected with *Hsp68* (top) or *2ankrd1aEN-Hsp68* (bottom) after I/R injury. (C) Cardiac average radiance normalized to the 7 dpi time point increased over time with *2ankrd1aEN* while remaining stable with *Hsp68* (n = 4 mice, Holm-Sidak multiple comparisons test). **(D)** Average cardiac radiance directed by *2ankrd1aEN* was significantly higher in mice with I/R injury compared to Sham at 7 dpi (n = 4 mice, Welch's t test). **(E)** Average cardiac radiance was more significantly elevated in the first 21 days post-injury in mice with I/R injury compared to sham (n = 4 mice, Mann-Whitney tests).

Figure 4. Screening of AAV libraries for enriched capsids in injured myocardium
(A) Schematic of AAV capsid library screening delivered systemically to mice with either sham (n = 1 mouse) or I/R (n = 2 mice) injury at 9 dpi. Two days later, hearts were biopsied to collect AAV genomes in either injured or remote tissues. **(B)** Capsid sequenced reads enriched in the injured tissues were plotted against sham animals. Each point represents a unique capsid. Wild-type AAV9 capsid is marked by blue arrow. **(C)** Representative fluorescence imaging of AAV9 (top) or variant capsid IR41 (bottom) delivering a self-complementary *CBA::EGFP* cassette at 16 dpi. Asterisks indicate infarct site, imaged at higher magnification in middle and right panel. Dashed white lines indicate the border zone region. Left scale bar, 1 mm. Middle and right scale bar, 100 um.

Figure 5. Post-injury delivery of AAV.IR41 variant capsid enhances *2ankrd1aEN*-directed expression in injured myocardium

(A) Representative IVIS images of mice with sham (top) or (bottom) surgery transduced with either AAV9 (left) or IR41 (right) packaged with *2ankrd1aEN-Hsp68::fLuc* (n = 3-4 mice). **(B, C)** Cardiac average **(B)** and maximum **(C)** radiance was elevated in MI mice transduced with IR41 compared to AAV9 (n = 3-4 mice, Holm-Sidak multiple comparisons test). **(D)** Viral genome quantification from heart tissues was elevated in MI mice injected with IR41 compared to AAV9 (n = 3-4 mice, Holm-Sidak multiple comparisons test).

SUPPLEMENTAL FIGURE LEGENDS

Figure S1. IVIS imaging for tracking spatiotemporal expression of rAAV vectors
(A) Schematic showing comparison of AAV9 vectors packaging either the strong, constitutively active *chicken beta actin* (*CBA*) promoter or minimal heat shock protein 68 (*Hsp68*) promoter to direct *fLuc* expression. n = 5 mice/AAV group. **(B)** Representative IVIS images of mice injected with AAV containing either *CBA* (top) or *Hsp68* (bottom) promoters. Red boxes indicate ROIs marking cardiac, liver, and whole-body expression. **(C)** Average radiance measured from cardiac ROIs from *CBA* (top) or *Hsp68* (bottom) promoters show relatively consistent expression from 30-68 days post-AAV injection. Square, male mice. Circle, female mice. **(D, E)** Average radiance measured from liver **(D)** and whole body **(E)** ROIs showed relatively consistent levels of expression over time for both promoters.

Figure S2. AAV.cc84 capsid retains cardiac tropism while minimizing liver transduction
(A) Representative IVIS images of mice injected with either AAV9 (left) or AAV.cc84 (right) at 7 (top) and 35 days (bottom) post-AAV injection. **(B)** Average radiance in the heart was similar between AAV9 and AAV.cc84 (n = 6 mice, Holm-Sidak multiple comparisons test). **(C)** Vector genome quantification from cardiac tissues showed similar levels of vector genomes between AAV9 and AAV.cc84 for both sexes (n = 3 mice, Holm-Sidak multiple comparisons test). **(D)** Representative IVIS images of mice with ROIs used to measure expression in head/neck and lower abdomen (white dashed box). **(E)** Average radiance measured in the head/neck (left) and lower abdomen (right) was similar between AAV9 and AAV.cc84 over the course of the study (n = 6 mice, Holm-Sidak multiple comparisons test).

Figure S3. Delivery of AAV.cc84 packaging 2ankrd1aEN after myocardial injury
(A) I/R surgery injury extent was assessed by ejection fraction via echocardiography to estimate injury prior to AAV delivery (n = 4 mice). **(B)** Cardiac average radiance plotted for each individual mouse with I/R injury plotted over time with either *Hsp68::fLuc* (gray) or *2ankrd1aEN-Hsp68::fLuc* (black). **(C)** Representative IVIS images of sham-operated mice injected with AAV.cc84 packaged with *2ankrd1aEN-Hsp68::fLuc*.

Figure S4. Screening AAV capsid libraries enriched in injured myocardium
(A) Injury site-enriched capsids in I/R-injured mice. Each point represents a unique capsid. Top left quadrant, capsids co-enriched at injury site. Wild-type AAV9 capsid is marked by an orange arrow. **(B)** Representative fluorescence imaging of variant capsids, IR42 (left) and IR43 (right), delivering a self-complementary *CBA::EGFP* cassette at 16 dpi. Asterisks indicate infarction area. Scale bar, 1 mm. **(C)** Immunofluorescence of infarct sites of mice transduced with either AAV9 (left) or IR41 (right) show no colocalization of EGFP and Vimentin. Scale bar, 100 um.

Figure S5. Post-injury delivery of variantAAV.IR41 variant capsid enhances *2ankrd1aEN*-directed expression in injured myocardium over AAV9
(A) Compiled IVIS images of mice that underwent sham or MI surgery with AAV9 or IR41 transduced at 3 dpi. Mice were imaged at 7, 14, and 21 dpi. **(B, C)** Cardiac average **(B)** and maximum **(C)** radiance were statistically similar between AAV9 and IR41 in sham-operated mice.

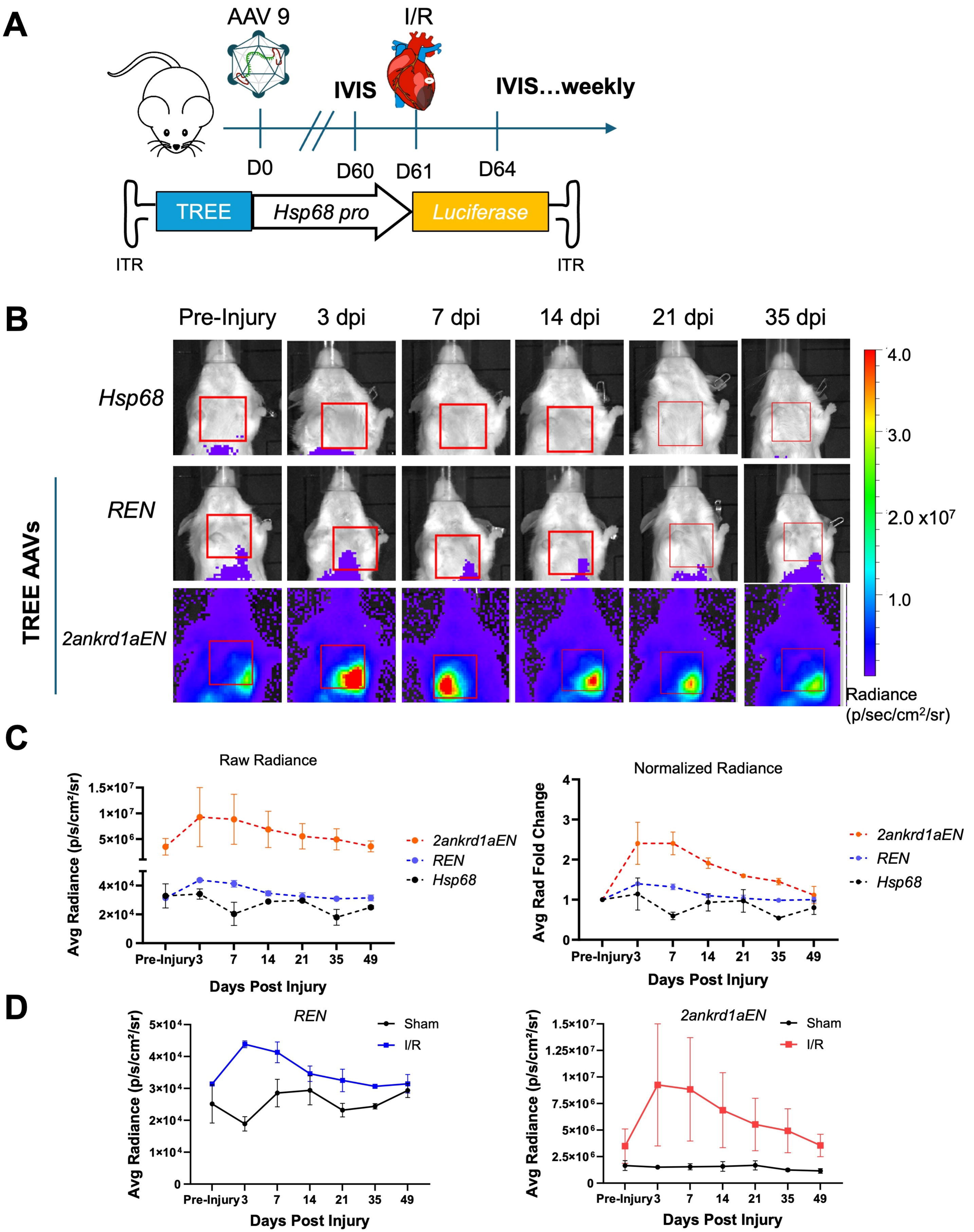
A
AAV 9
I/R
IVIS
IVIS…weekly
D0
D60
D61
D64
TREE
Hsp68 pro
Luciferase
ITR
ITR
B
Pre-Injury
3 dpi
7 dpi
14 dpi
21 dpi
35 dpi
Hsp68
REN
2ankrd1aEN
TREE AAVs
4.0
3.0
2.0 x10^7
1.0
Radiance (p/sec/cm²/sr)
C
Raw Radiance
Avg Radiance (p/s/cm²/sr)
1.5×10^7
1×10^7
5×10^6
4×10^4
2×10^4
0
Pre-Injury 3 7 14 21 35 49
Days Post Injury
2ankrd1aEN
REN
Hsp68
Normalized Radiance
Avg Rad Fold Change
4
3
2
1
0
Pre-Injury 3 7 14 21 35 49
Days Post Injury
2ankrd1aEN
REN
Hsp68
D
REN
Sham
I/R
Avg Radiance (p/s/cm²/sr)
5×10^4
4×10^4
3×10^4
2×10^4
1×10^4
0
Pre-Injury 3 7 14 21 35 49
Days Post Injury
2ankrd1aEN
Sham
I/R
Avg Radiance (p/s/cm²/sr)
1.5×10^7
1.25×10^7
1×10^7
7.5×10^6
5×10^6
2.5×10^6
0
Pre-Injury 3 7 14 21 35 49
Days Post Injury

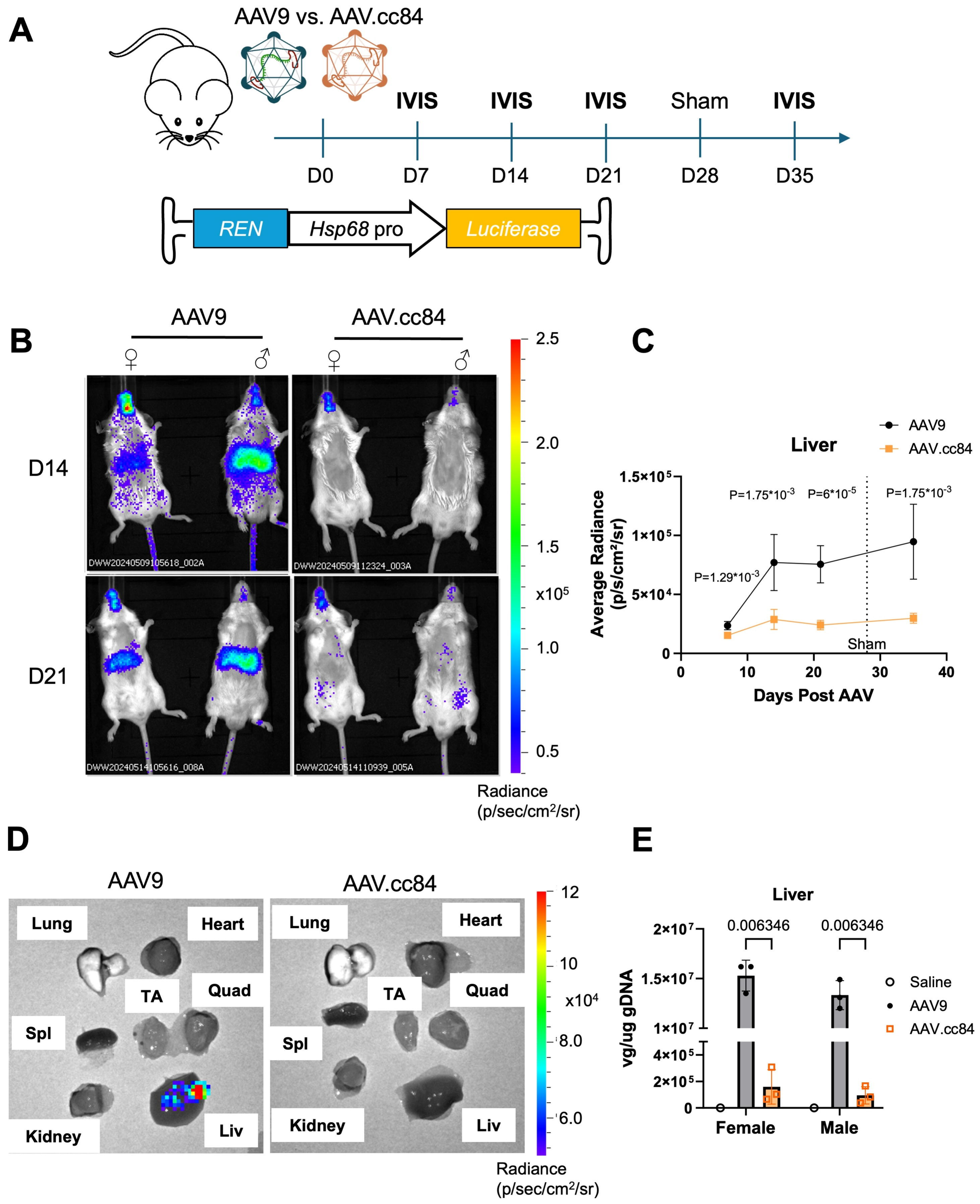
A
AAV9 vs. AAV.cc84
IVIS
IVIS
IVIS
Sham
IVIS
D0
D7
D14
D21
D28
D35
REN
Hsp68 pro
Luciferase
B
AAV9
AAV.cc84
♀
♂
♀
♂
D14
D21
DWW20240509105618_002A
DWW20240509112324_003A
DWW20240514105616_008A
DWW20240514110939_005A
2.5
2.0
1.5
x10^5
1.0
0.5
Radiance
(p/sec/cm²/sr)
C
Liver
AAV9
AAV.cc84
Average Radiance
(p/s/cm²/sr)
1.5×10^5
1×10^5
5×10^4
0
P=1.75*10^-3
P=6*10^-5
P=1.75*10^-3
P=1.29*10^-3
Sham
0
10
20
30
40
Days Post AAV
D
AAV9
AAV.cc84
Lung
Heart
TA
Quad
Spl
Kidney
Liv
Lung
Heart
TA
Quad
Spl
Kidney
Liv
12
10
x10^4
8.0
6.0
Radiance
(p/sec/cm²/sr)
E
Liver
0.006346
0.006346
vg/ug gDNA
2×10^7
1.5×10^7
1×10^7
4×10^5
2×10^5
0
Saline
AAV9
AAV.cc84
Female
Male

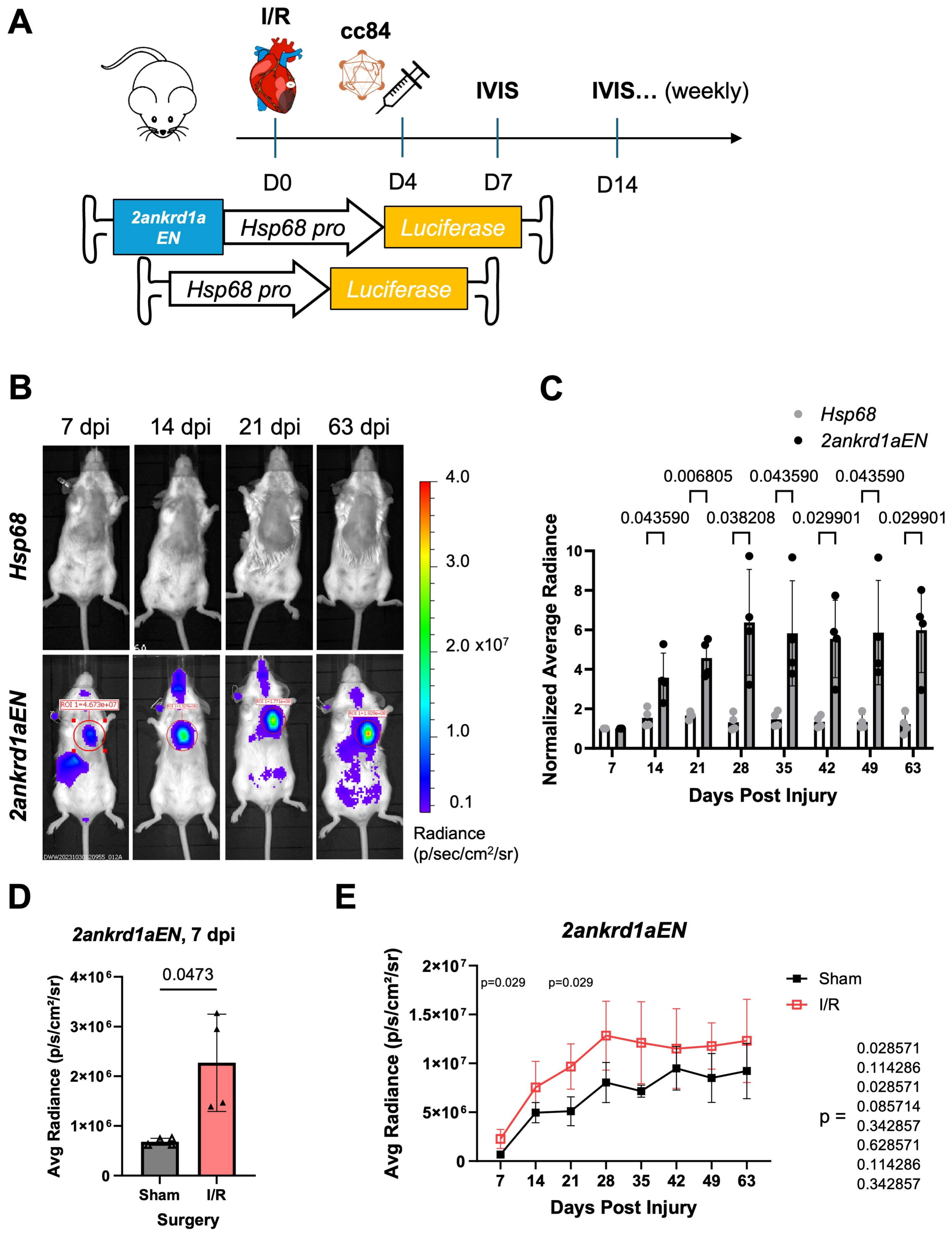
A
I/R
cc84
IVIS
IVIS… (weekly)
D0
D4
D7
D14
2ankrd1a EN
Hsp68 pro
Luciferase
Hsp68 pro
Luciferase
B
7 dpi
14 dpi
21 dpi
63 dpi
Hsp68
2ankrd1aEN
ROI 1=4.673e+07
4.0
3.0
2.0 x10^7
1.0
0.1
Radiance (p/sec/cm²/sr)
C
Hsp68
2ankrd1aEN
0.006805
0.043590
0.043590
0.043590
0.038208
0.029901
0.029901
Normalized Average Radiance
Days Post Injury
D
2ankrd1aEN, 7 dpi
0.0473
Avg Radiance (p/s/cm²/sr)
Sham
I/R
Surgery
E
2ankrd1aEN
p=0.029
p=0.029
Avg Radiance (p/s/cm²/sr)
Sham
I/R
p =
0.028571
0.114286
0.028571
0.085714
0.342857
0.628571
0.114286
0.342857
Days Post Injury

A

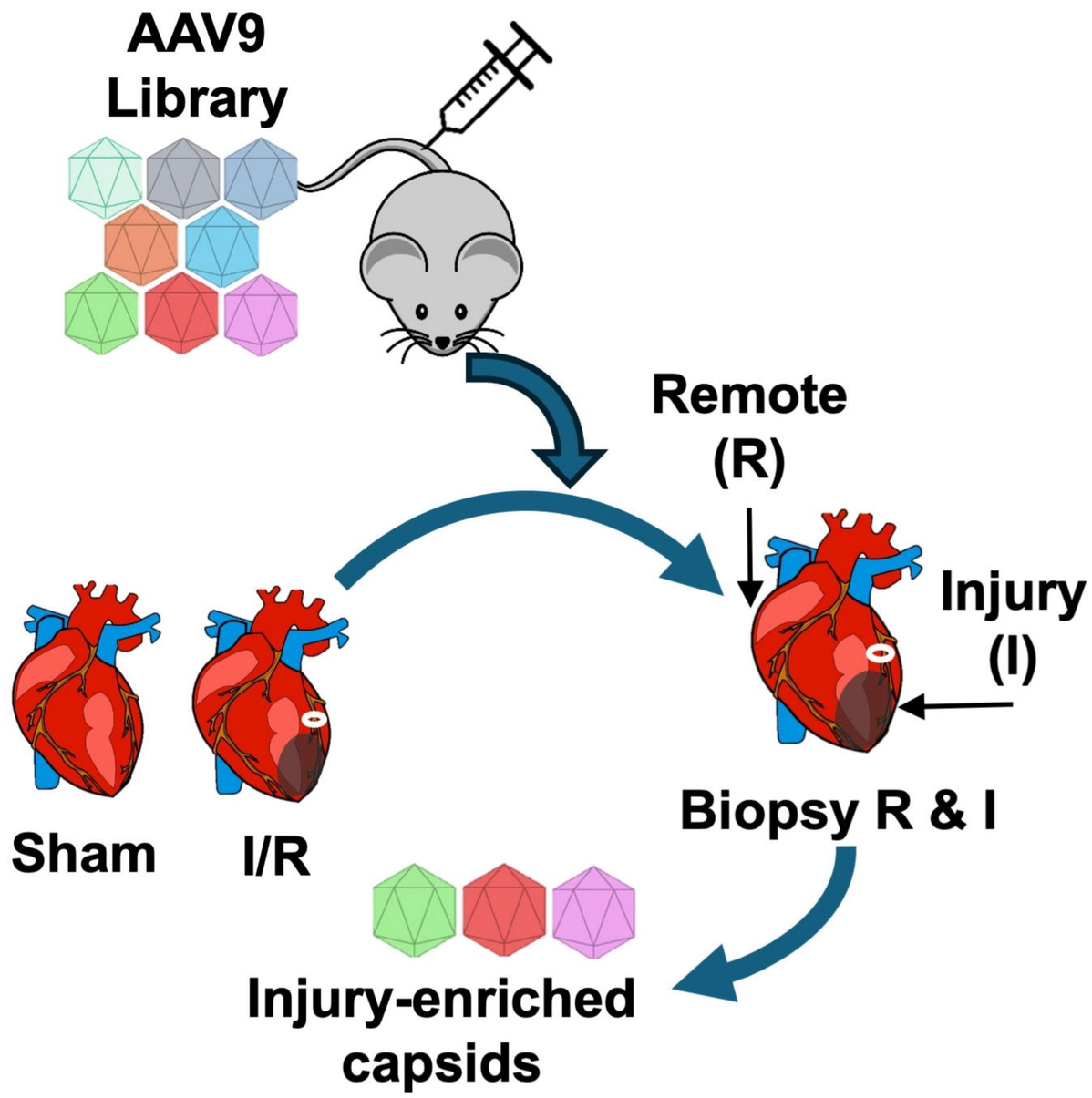
AAV9
Library
Remote
(R)
Injury
(I)
Sham
I/R
Biopsy R & I
Injury-enriched
capsids

B

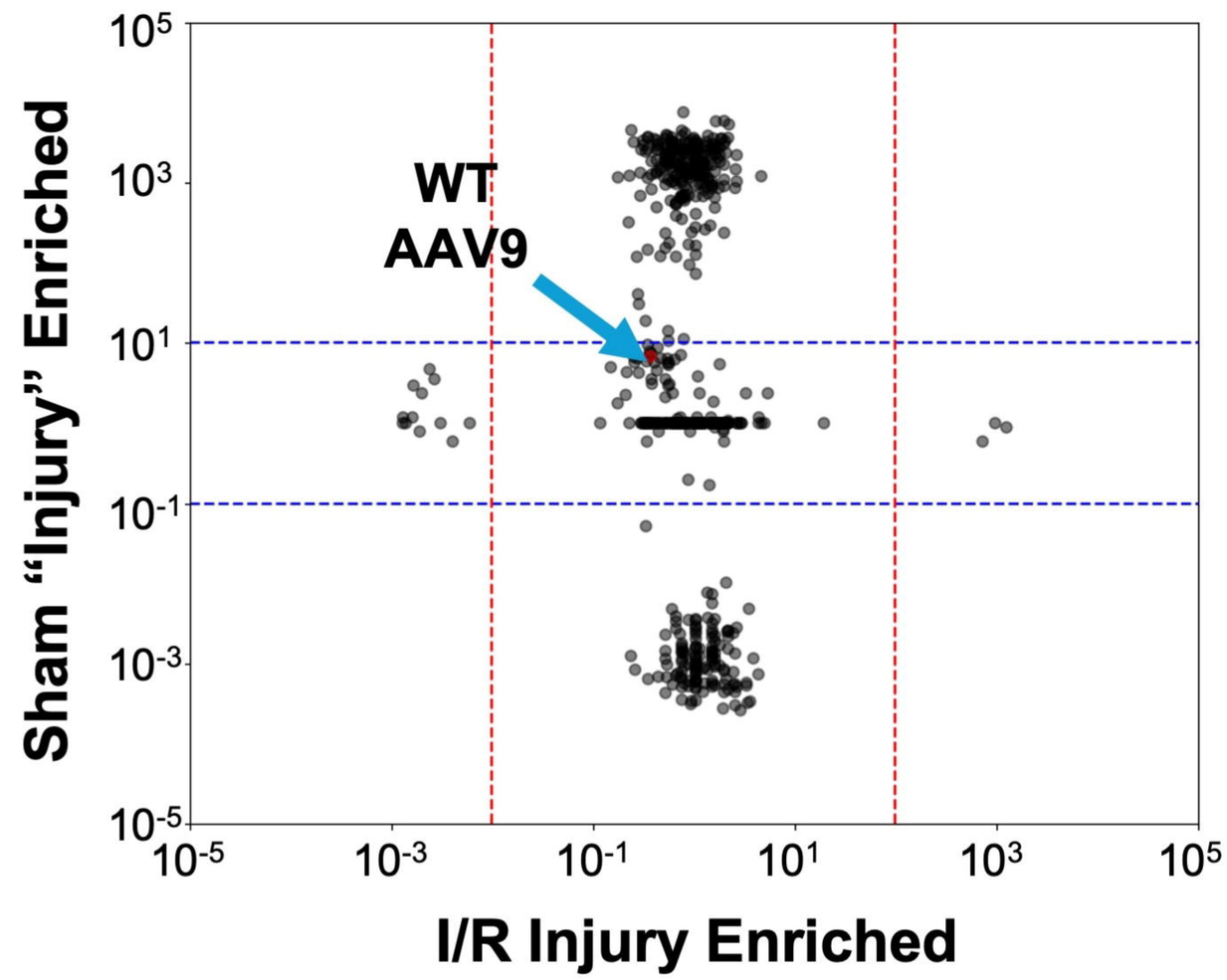
WT
AAV9
Sham "Injury" Enriched
I/R Injury Enriched
10^{5}
10^{3}
10^{1}
10^{-1}
10^{-3}
10^{-5}

C

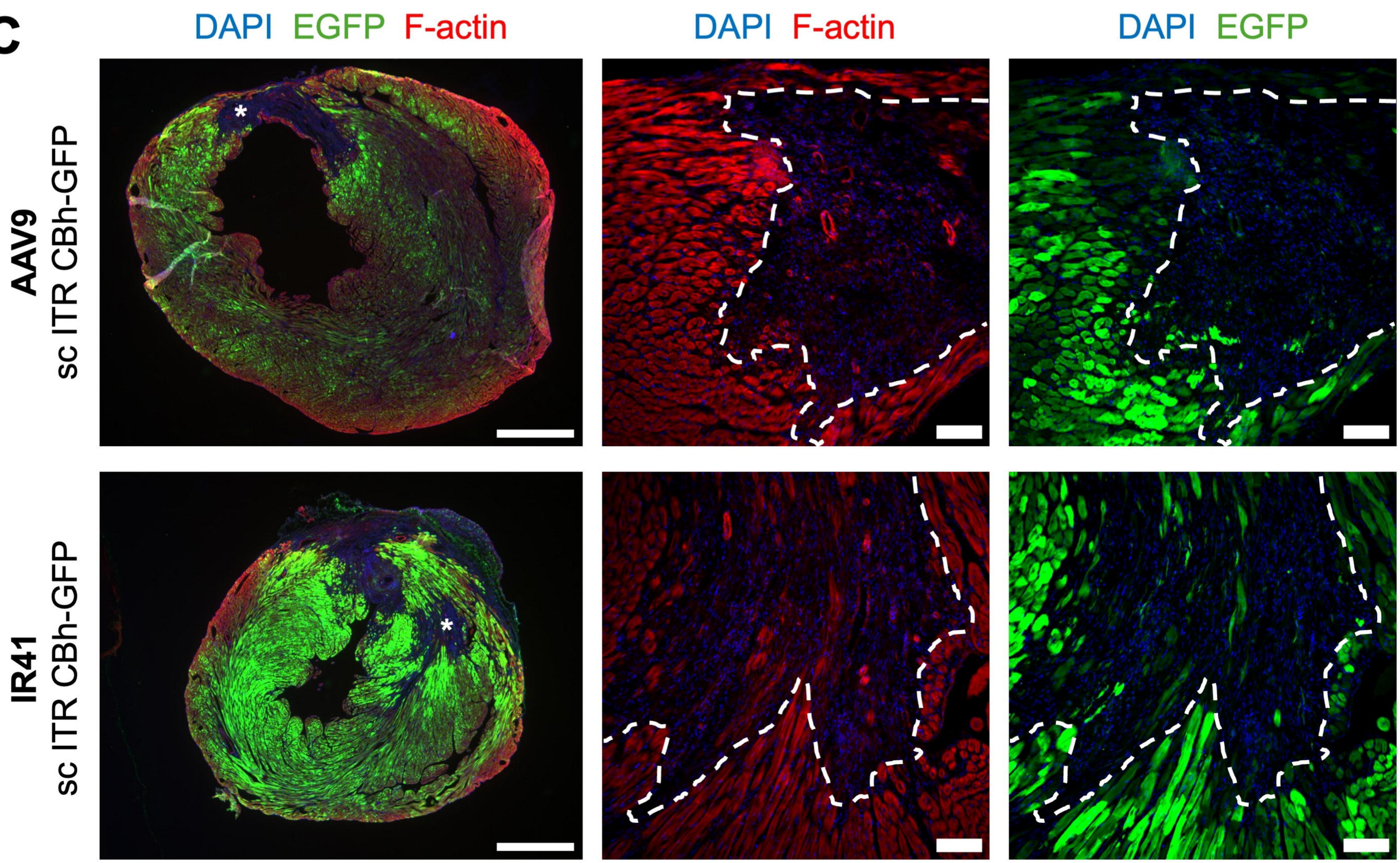
DAPI EGFP F-actin
DAPI F-actin
DAPI EGFP
AAV9
sc ITR CBh-GFP
IR41
sc ITR CBh-GFP
*
*

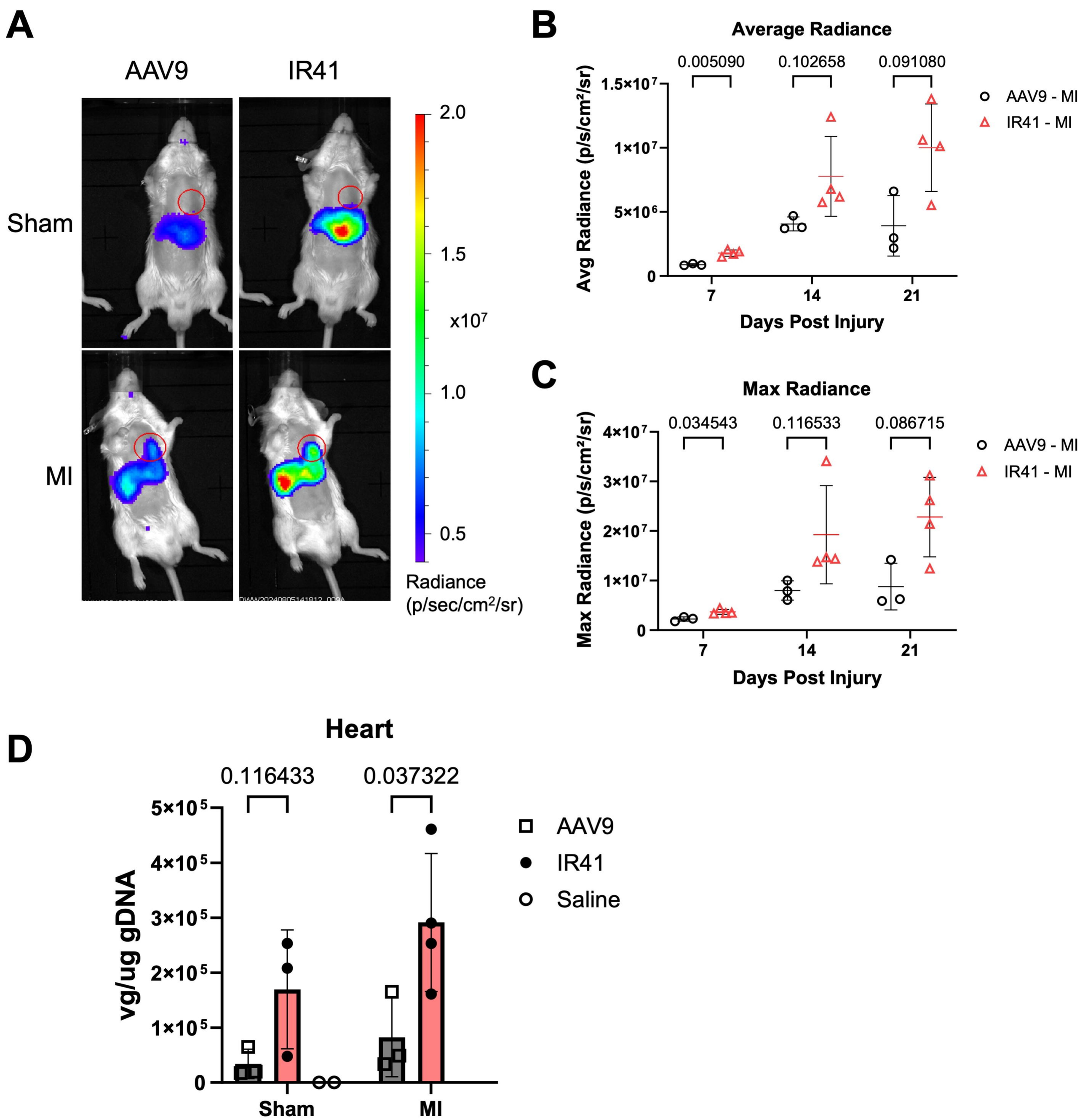
A
AAV9
IR41
Sham
MI
2.0
1.5
x10^7
1.0
0.5
Radiance (p/sec/cm²/sr)
B
Average Radiance
0.005090
0.102658
0.091080
Avg Radiance (p/s/cm²/sr)
1.5×10^7
1×10^7
5×10^6
0
7
14
21
Days Post Injury
AAV9 - MI
IR41 - MI
C
Max Radiance
0.034543
0.116533
0.086715
Max Radiance (p/s/cm²/sr)
4×10^7
3×10^7
2×10^7
1×10^7
0
7
14
21
Days Post Injury
AAV9 - MI
IR41 - MI
D
Heart
0.116433
0.037322
vg/ug gDNA
5×10^5
4×10^5
3×10^5
2×10^5
1×10^5
0
Sham
MI
AAV9
IR41
Saline